Extensive study of radiation dose on human body at aviation altitude through Monte Carlo simulation

Abhijit Roy[a], Ritabrata Sarkar[a,*], Choonsik Lee[b]

[a]*Indian Centre for Space Physics, 43 Chalantika, Garia Station Rd., Kolkata 700084, W.B., India*
[b]*Division of Cancer Epidemiology and Genetics, National Cancer Institute, National Institutes of Health, Bethesda, MD 20852, USA*

Abstract

The diverse near-Earth radiation environment due to cosmic rays and solar radiation has direct impact on human civilization. In the present and upcoming era of increasing air transfer, it is important to have precise idea of radiation dose effects on human body during air travel. Here, we calculate the radiation dose on the human body at the aviation altitude, also considering the shielding effect of the aircraft structure, using Monte Carlo simulation technique based on Geant4 toolkit. We consider proper 3D mathematical model of the atmosphere and geomagnetic field, updated profile of the incoming particle flux due to cosmic rays and appropriate physics processes. We use quasi-realistic computational phantoms to replicate the human body (male/female) for the effective dose calculation and develop a simplified mathematical model of the aircraft (taking Boeing 777–200LR as reference) for the shielding study. We simulate the radiation environment at the flying altitude (considering geomagnetic latitude in the range of 45-50°), as well as at various locations inside the fuselage of the aircraft. Then, we calculate the dose rates in the different organs for both male and female phantoms, based on latest recommendations of International Commission on Radio logical Protection. This calculation shows that the sex-averaged effective dose rate in human phantom is 5.46 μSv/h, whereas, if

---

*Corresponding author

Email addresses: `ritabrata.s@gmail.com` (Ritabrata Sarkar), `aviatphysics@gmail.com` (Ritabrata Sarkar)

we calculate weighted sum of equivalent dose contributions separately in female and male body: total weighted sum of equivalent dose rate received by the female phantom is 5.72 μSv/h and that by the male phantom is 5.20 μSv/h. From the simulation, we also calculate the numerous cosmogenic radionuclides produced inside the phantoms through activation or spallation processes which may induce long-term biological effects.

Keywords: Radiation dose, Galactic Cosmic Ray, Atmospheric radiation, Radiation dose at aviation altitude

---

1. Introduction

Two major inputs controlling the near Earth space radiation environment are Galactic Cosmic Radiation (GCR) and Solar Particle Events (SPEs). The particles and radiation have a wide energy range spanning from few MeV to above 10^{12} GeV with decreasing flux as the energy increases. The nature and origin of these particles depend on their energy. The low energy radiation observed below about 100 MeV are mainly from solar origin. However, during the SPEs (Reames, 1999) the energy of the solar particles or radiation due to coronal mass ejection or solar flares, can extend up to several GeVs and the flux can last from an hour to days (Gopalswamy et al., 2006). On the other hand, GCRs of Galactic or extra-galactic origin, while propagating through the heliosphere, interact with the electromagnetic field carried by the solar energetic particles, which modifies the intensity of low energy GCR particles up to the energy of several GeVs (Gaisser, 1990). The heliospheric space-radiation environment is highly dynamic and strongly correlated with solar activities.

The intensity of space radiation near Earth depends on the strength and spatial distribution of Earth's magnetic field (Störmer, 1955). The charged particle (spectral and spatial) distribution is modified by the geomagnetic field surrounding the Earth which also depends on the solar activity. There is a strong dependence of the rigidity cut-off of the primary GCR and SPE particles on the geomagnetic latitude and solar activity (Bazilevskaya & Svirzhevskaya,

1998; Sarkar et al., 2017). After entering the Earth's atmosphere, the radiation and particles interact with the atmospheric molecules, producing a large number of secondary particles in cascade, which is known as extensive air shower. Due to the balance between the production rate of the secondary particles and their absorption in the atmosphere, the particle flux has a maximum at around 15-20 km altitude (also depends on the geomagnetic latitude), which is called the Regener-Pfotzer maximum (Regener & Pfotzer, 1934). The particle flux starts to decrease below this region.

The radiation environment in the atmosphere due to the primary Cosmic Ray (CR) particles can produce serious biological hazard to high altitude travelers and also can disrupt the microelectronics components in the aircraft. The radiation intensity and hence the induced potential hazard generally increases with altitude and geomagnetic latitude. The CR particles and radiation have enough energy to give a serious amount of radiation dose on human body which may lead to fatal cancer, eye cataracts, cardiovascular diseases, malfunctions of the central nervous system etc. From the study of Bennett et al. (2013) on Air Canada pilots shows that, most of them received annual dose about 3 mSv even a few of them received approx 5 mSv, which is higher than the International Commission on Radiological Protection (ICRP) recommended 1 mSv per year limit for public radiation exposure. Due to this high exposure from CR on flight crews, disorder in the reproductive system and high risk of miscarriage among female flight attendants was also observed (Grajewski et al., 2015; Lauria et al., 2006; Aspholm et al., 1999). For these reasons pilots and flight crews are considered as radiation workers by ICRP (ICRP, 2007). Continuous exposure to this kind of radiation can also produce various radioactive isotopes in our body (Brodzinski et al., 1969), where these could cumulatively give radiation dose depending upon their half lives.

There are different protection and operational quantities used in radiation dosimetry like: *equivalent dose* (H_T) (in different organ type T), *effective dose* (E) and *ambient dose equivalent* ($H^*(10)$). The definition of these quantities can be found in ICRP publication 103 (ICRP, 2007). As the protection quantities

like E, H_T cannot be measured directly in the human body, so the operational quantity ($H^*(10)$) is used for measurements, from which the protection quantities can be derived using suitable conversion coefficient. However, in many cases ambient dose equivalent cannot properly estimate the effective dose (Ferrari et al., 1997; Sato et al., 1999).

There are different computer programs based on Monte Carlo calculation or empirical models to calculate radiation dose at flight altitude (Bottollier-Depois et al., 2012). But there are significant number of uncertainties associated with these kind of calculations which is summarized in ICRU (2010) and EURADOS report (Lindborg et al., 2004a). Also, there are a limited number of studies that consider the effect of aircraft structure for dose calculation (Battistoni et al., 2005; Ferrari et al., 2004; Dyer et al., 2003; Dyer & Lei, 2001). These calculations also have several limitations associated with them like, considering the isotropic distribution for fluence to dose calculation and fixed vertical cut-off rigidity instead of direction dependence of cut-off rigidity.

There is no experimental or calculated radiation dose data at individual organs of flight crews and a few study on the shielding effect of aircraft structure. These studies can be important for planning the radiological protection. In this concern, we develop a computer simulation program based on Geant4 (Agostinelli et al., 2003) Monte Carlo simulation toolkit to calculate the absorbed dose rate, equivalent dose rate in individual organs, organ weighted sum of equivalent dose rate for both male and female body as well as the sex-average effective dose rate at aviation altitude radiation environment. The change in particle fluxes inside the aircraft due to the shielding effects of the aircraft structure also have been studied here considering full-scale aircraft model.

In the following Sec. 2, we describe the simulation method for the calculation of radiation dose at the aviation altitude. We present and discuss the simulation results in Sec. 3. And finally conclude in Sec. 4.

4

2. Simulation Method for Dose Calculation

The overall simulation of radiation dose at flight altitude comprises a series of calculations. First, we calculated the radiation environment at the relevant altitude for which we need to consider proper models for the Earth's atmosphere, geomagnetic field and distribution of the primary GCR. To simulate the radiation environment inside the aircraft, we need to consider a proper structure of the aircraft. Similarly, to calculate the radiation dose in human body, proper computational description of the human phantom is required. We also need to consider the underlying physics processes properly to define the radiation interactions with matter.

2.1. Simulation of secondary radiation environment in atmosphere

The secondary CR radiation environment at the Earth's atmosphere is formed due to the interaction of primary GCR with Earth's atmosphere. Here, in this work we did not consider the sporadic effects due to the high energy particles from SPE. A detailed description of the simulation procedure for primary GCR interaction with the Earth's atmosphere to produce secondary radiation and particle fluxes can be found in Sarkar et al. (2020). For this simulation purpose, we considered full 3D atmospheric and magnetospheric models and with updated Local Interstellar Spectrum (LIS) (Herbst et al., 2017) for the primary GCR. We used NRLMSIS-00 (Picone et al., 2002) atmospheric model to define the Earth's atmosphere up to 100 km altitude from the surface subdivided into 100 concentric shells with thickness equal in logarithmic scale. The Earth's magnetosphere was defined using: (i) 12th generation IGRF model (Thébault et al., 2015) for the inner magnetic field distribution and (ii) Tsyganenko Model (Tsyganenko & Andreeva, 2016) for the external magnetic field distribution, with proper input parameters.

A proper description of primary GCR LIS is very important in order to simulate the shower of secondary particles in the Earth's atmosphere. At the end of 2012, for the first time *in situ* measurement of unmodulated primary

GCR was possible by *Voyager1* (Stone et al., 2013) after crossing the heliopause. Complimenting the PAMELA (Adriani et al., 2013) and AMS-02 (Aguilar et al., 2015) measurements with the *Voyager1* measurement, a new model of very LIS, before modulation by the heliospheric electromagnetic field, was proposed by Vos & Potgieter (2015). This LIS model was used to derive the differential GCR flux at 1 AU by Herbst et al. (2017) based on forced-field approximation (Caballero-Lopez & Moraal, 2004; Moraal, 2013). We considered this model to describe the GCR flux at the top of the atmosphere with an arbitrary value for the solar modulation potential $\phi = 524$ MV, (which corresponds to a solar transitional phase from maximum to nearing a minimal activity).

The rigidity cut-off for the CR charged particles imposed by the geomagnetic field distribution is an important factor for the calculation of secondary radiation environment in the atmosphere. While, most of the other similar program consider the vertical rigidity cut-off for the distribution of the primary GCR at different locations, we considered the back-tracing method to select the allowed tracks into the atmosphere from the isotropic distribution of particles at the top of the atmosphere (Sarkar et al., 2020). This method takes care of the directional dependence and penumbra region of the rigidity cut-off. However, for an example, Fig. 1 exhibits the positional distribution of vertical rigidity cut-off at 10 km altitude. Due to high rigidity cut-off at the geomagnetic equator, only the charged particles with enough rigidity can penetrate the Earth's magnetic field and interact with the atmospheric nuclei, while the neutral particles are unaffected.

Using the geomagnetic field model and back-tracing method, the position dependent geomagnetic modulation was inherently achieved in the simulation as can be seen from Fig. 2. This plot shows primary GCR spectra (for protons and alpha particles) at an altitude of 400 km, averaged over two different geomagnetic latitude ranges 0-63.03° and 0-80.21°, along with the very LIS at 122 AU and modified LIS at 1 AU (modulated by the electromagnetic field carried by the solar wind). We recorded all the relevant information like: position, momentum, energy, type (pdg number) etc. of the generated secondary particles
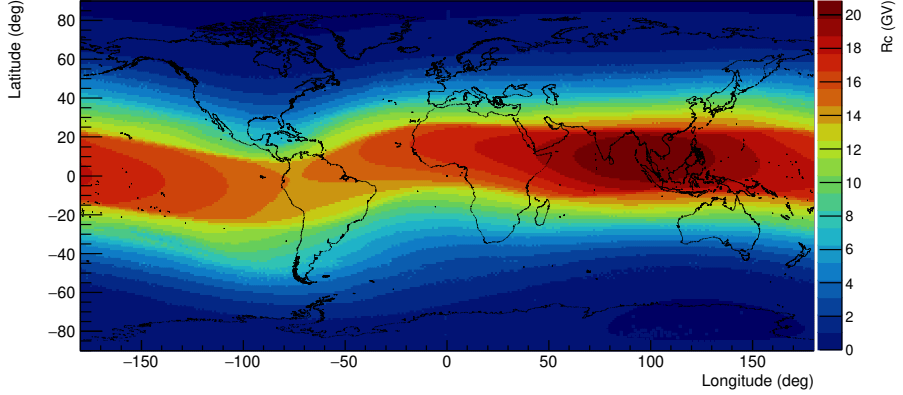
6

Figure 1: Distribution of vertical rigidity cut-off at 10 km altitude over the total geographic region.

and radiation in this step of the simulation to be used afterward.

2.2. Human phantom and aircraft model

In the next stage of the calculation, we simulated the interaction of secondary radiations produced in the atmosphere (along with the primaries survived the geomagnetic cut-off) in the human body and with the aircraft to see the structural effects on radiation dose.

The simulation of radiation dose received by human organs has been done considering UF/NCI hybrid phantom models (PHANTOMS library), jointly developed by the University of Florida and National Cancer Institute. These computational models contain more than 100 organs or tissues. More details about PHANTOMS and their compositions can be found in Lee et al. (2009); Griffin et al. (2019) and references therein. We can calculate the energy depositions separately in each of the organs and subsequently get the overall effective dose in human body.

To find out the variation of radiation fluxes inside the aircraft structure, we developed a simplified mass model of the aircraft structure in Geant4 simulation framework, based on Boeing 777–200LR (Boeing Co., 2020) aircraft model. We sampled the radiation effects at different positions inside the aircraft by placing
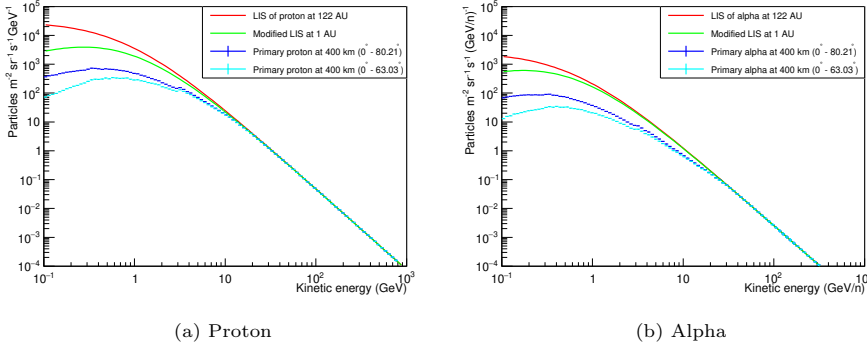
(a) Proton   (b) Alpha

Figure 2: Very LIS of primary GCR in interstellar medium (red); modulated primary GCR in heliosphere at 1 AU (green); modulated primary GCR by magnetosphere at 400 km in two different geomagnetic latitude range (blue, cyan).

dummy volumes (three spheres of 2 m diameter at the front, middle and back sections of the fuselage). A representative picture of the aircraft model along with the dummy spheres can be seen in Fig. 3. A simplified description of the jet fuel, window glass, cockpit instrumentation has been considered. For the aircraft structure construction, we mainly used 5 mm thick aluminum (1.35 g/cm^2) and the composition and density of other different materials (jet fuel, window glass, cockpit instrumentation) were taken from Ferrari et al. (2004). The full tanks of fuel (145,000 kg) were placed inside the wings and lower half of the fuselage confined along only in the region where the wings are connected to the fuselage. An additional aluminum plate of 5 mm thickness comprised the floor of the passenger cabin, thus rendering a total equivalent thickness of 2.7 g/cm^2 for the upward going particles.

2.3. Physics list considered in the simulation

It is important to consider the right set of physics processes to describe the radiation interactions with the atmosphere, aircraft structure and human phantom. For this simulation, we considered *QGSP_BIC_AllHP* physics list (Geant4, 2020) with updated *TALYS-based Evaluated Nuclear Data Library (TENDL)*, which is appropriate for hadronic interaction and isotope productions. To han-
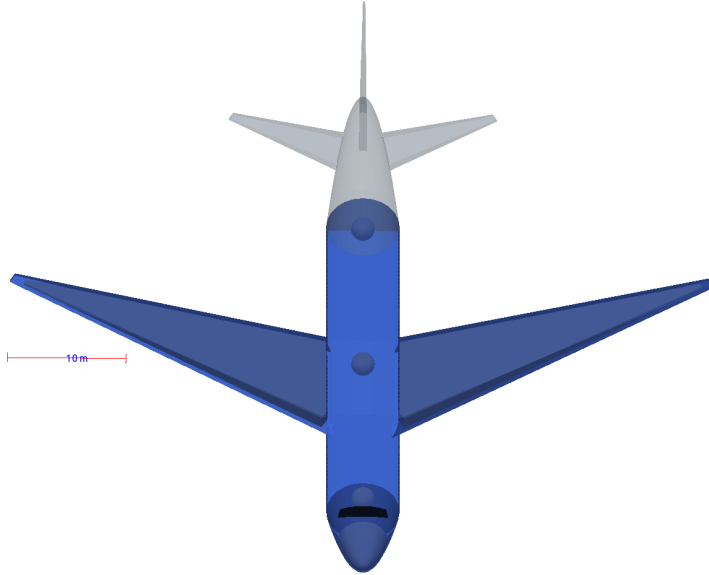
8

Figure 3: Mass model structure of the aircraft used in the simulation with three sampling dummy spheres placed at different sections inside the fuselage.

dle electromagnetic interactions, *electromagnetic_options3* physics list was used, which is suitable for space and medical purposes.

2.4. Simulation of radiation interaction in human phantom and aircraft structure

From the knowledge of radiation environment at the flight altitude, we simulated the radiation interactions in the human phantoms and the aircraft structure. First, to calculate the radiation effect in human body we irradiated the phantoms with different secondary GCR particles from upper and lower hemispheres of 2 m radius (without considering the aircraft structure) for both upward and downward going particles and calculated the corresponding deposited doses. We used the standing posture of the phantoms for irradiation, since there is no significant difference in radiation doses observed in the sitting and standing postures (Alves et al., 2016).

To find out the variation of radiation inside the aircraft due to shielding effects of aircraft structure, we irradiated the aircraft from two hemispheres

9

with 35 m radius along with three dummy spheres inside the fuselage at different locations shown in Fig. 3 and recorded the information of each event inside those spheres.

For the purpose of radiation dose calculation in human body, we irradiated both male and female phantoms by 10^6 number of each different types of particles; while for the simulation of radiation interactions in the aircraft, we considered 10^7 particles from both upper and lower hemispheres. For both simulations, we considered the particles with kinetic energy distribution in the range of 10 keV to 800 GeV for downward going particles, while for upward going particles the energy range is 10 keV to 10 GeV. This choice of energy ranges can be justified by the simulated outcome of the secondary particle fluxes in the atmosphere discussed later in Sec. 3.1.

3. Results and Discussions

3.1. Radiation at flight altitude

The primary GCR LIS is modified in the heliosphere, by the electromagnetic field carried by the solar wind. At Earth's vicinity, this modified GCR is further modulated by the Earth's magnetic field, while propagating towards Earth through the magnetosphere. The primary particles with modified flux then interact with the atmospheric nuclei to produce secondary particles and radiation which in turn interact with the aircraft structure. The flux distribution of all the different particles generated from the simulation at the flight altitude (which we considered here at 10 km from the Earth's surface) is shown in Fig. 4. Though, due to the lack of direct experimental measurements of the distribution of radiation flux components at aviation altitude, it is not possible to directly verify the results shown in this figure. Nevertheless, we compared the simulation results at satellite altitude with AMS observation of proton flux and at balloon altitude with the atmospheric radiation measurement by ICSP balloon borne experiment (Sarkar et al., 2020). Ferrari et al. (2005) mentioned the anisotropy in the distribution of high energy radiation flux components for
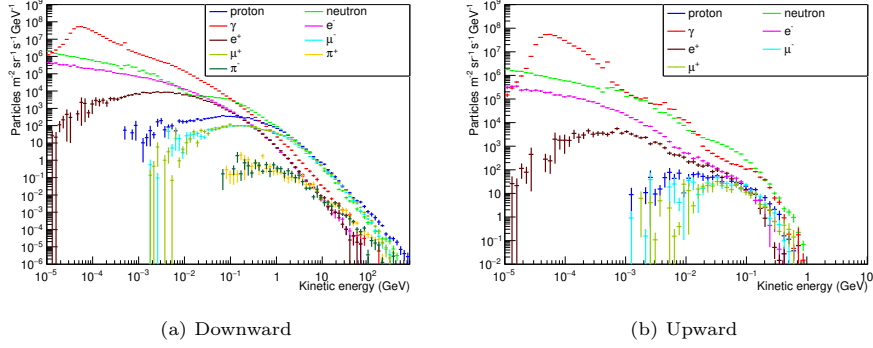
10

Figure 4: Different secondary CR particle fluxes at 10 km altitude in the geomagnetic latitude range of ∼45°–50° for both downward and upward going particles with respect to local zenith.

downward and upward particles at aviation altitude, while low energy neutrons and photons < 10 MeV are more isotropically distributed. This fact is also evident from Fig. 4 and also can be seen at balloon altitude as shown in Sarkar et al. (2020).

For the current purpose, we consider the fluxes of proton, neutron, γ, e^-, e^+, μ^-, μ^+, π^- and π^+ generated from primary GCR interactions with atmosphere. In this simulation, we do not consider the weakly interacting (e.g. neutrinos) and low abundant (K^-, K^+, $\overline{p}$, $\overline{n}$ and others) particles, we also neglect π^-, π^+ for upward and π^o for both directions due to their low flux. The atmospheric radiation calculations were done at 10 km altitude (which is the typical cruise altitude of commercial aircraft, e.g., FL328) and in ∼45°–50° geomagnetic-latitude (θ_M) region, since most frequent flight paths pass through this region (ICAO, 2016).

The dose calculation at other regions and altitudes can be done in the same way and will be considered in future. However, the latitudinal and longitudinal distribution of all the simulated atmospheric particles at 10 km altitude can be seen from Fig. 5 over the whole geographic region.
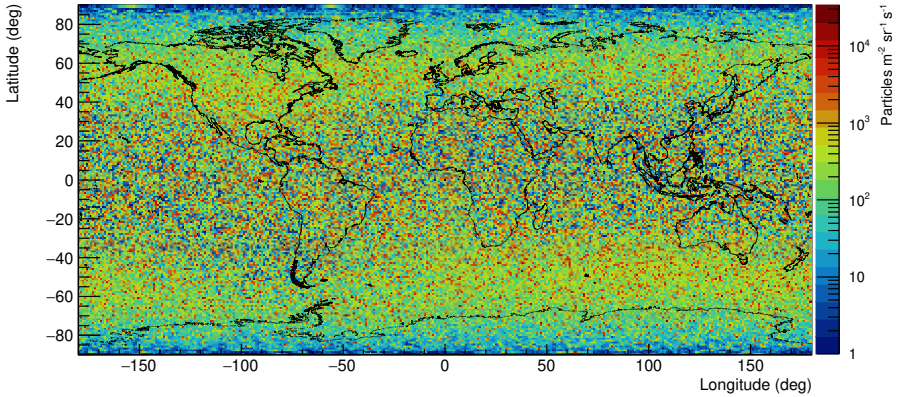
11

Figure 5: Positional distribution of all the simulated particles and radiation in the atmosphere at 10 km altitude over the whole geographic region.

3.2. Dose calculation in human body

Here in this study, we are to calculate the effective dose (E), equivalent dose (H_T) and absorbed dose ($D_{R,T}$) rates in human body from radiation interactions at aviation altitude, where T refers to particular organ or tissue type and R refers to type of radiation. The effective dose is calculated according to the equation:

$$E = \sum_T w_T H_T = \sum_T w_T \sum_R w_R D_{R,T}, \tag{1}$$

where w_T is the weighting factor for organ T ($\sum_T w_T = 1$), w_R is radiation weighting factor and $D_{R,T}$ is absorbed dose averaged over the organ T for particular radiation type R. The absorbed dose $D_{R,T}$ is the energy deposited per unit mass.

The ICRP first introduced the set of w_R values in ICRP (1991), which was updated by a new value for proton and introducing more accurate energy dependent continuous function of w_R instead of a step function for the neutrons in ICRP (2007). But the consideration of constant w_R values for proton and other CR ions may not be correct at higher altitudes where the energy and flux of these particles are higher (Banjac et al., 2019).

We calculated the total effective dose, as well as the individual contribu-

12

tions from different omnidirectional radiation and particles of atmospheric CRs mentioned in Sec. 3.1. The individual contributions from different radiation components to the weighted sum of equivalent dose rate is plotted in Fig. 6 for both male and female phantom along with their relative contributions to the total weighted sum of equivalent dose rate. The same values of weighted sum of equivalent dose rates along with their relative contributions are tabulated in Table 1, separated for downward and upward components of incident radiations. This calculation shows that most of the weighted sum of equivalent dose received by the phantom is due to the downward going particles (more than $\sim$95%), where maximum contribution comes from neutrons followed by proton, γ, $e^{\pm}$, $\mu^{\pm}$ and $\pi^{\pm}$.

ICRP (2007) defined the sex-averaged effective dose for reference person as:

$$E_{ref} = \sum_T w_T \left(\frac{H_T^M + H_T^F}{2} \right), \tag{2}$$

H_T^M and H_T^F being the equivalent dose in different organs of male and female body respectively. Since, the w_T factor for both male and female body in similar organs are considered same, Eqn. 2 can be rewritten as:

$$E_{ref} = \frac{\sum_T w_T H_T^M + \sum_T w_T H_T^F}{2}, \tag{3}$$

which is the average of weighted sum of equivalent dose of reference male and female. So, for the sake of comparison, we first calculated the total weighted sum of equivalent dose rates in reference female and male phantoms and then took the average to calculate the sex-averaged total effective dose rate.

Spatial distribution (frontal and side-wise view) of absorbed dose rate and equivalent dose rate inside both male and female phantoms are plotted in Fig. 7 and 8. The contributions to absorbed dose rates and equivalent dose rates from different primary incident particles in each organs, for both male and female phantom, are also shown in Fig. 9, 10 and 11, 12. Under the same irradiation condition, the dose received by the female phantom is slightly higher than the male phantom. Noticeable difference in radiation dose rates at different organs is quite apparent from these plots. Lund & Jevremovic (2019) also find similar
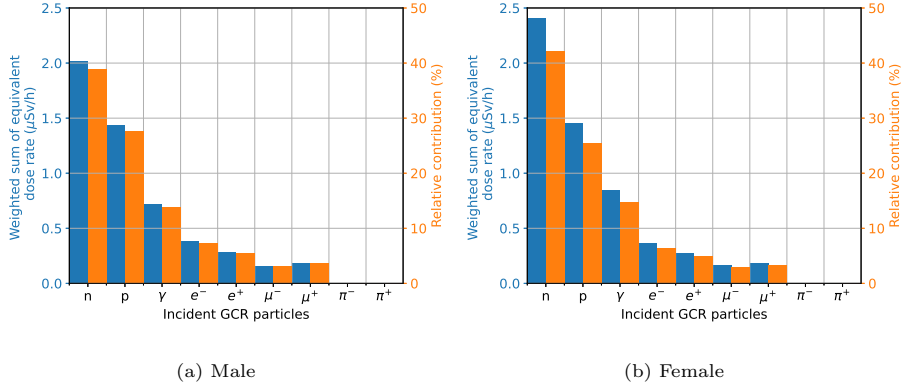
(a) Male   (b) Female

Figure 6: Weighted sum of equivalent dose rates and their relative contributions in male and female phantoms due to different incident secondary CR particles and radiation.

Table 1: Weighted sum of equivalent dose rates [and their relative contributions] for different incident particles and generated secondary particles in human (male/female) phantom for both downward and upward going particles.

Particles	Male ($\mu Sv/h$) [%]		Female ($\mu Sv/h$) [%]	
	Down	Up	Down	Up
n	1.841 [35.35]	0.180 [3.46]	2.246 [39.26]	0.163 [2.85]
p	1.434 [27.53]	0.008 [0.15]	1.446 [25.27]	0.009 [0.15]
γ	0.693 [13.32]	0.025 [0.48]	0.819 [14.32]	0.024 [0.42]
e^-	0.377 [07.23]	0.004 [0.09]	0.363 [06.35]	0.004 [0.08]
e^+	0.280 [05.37]	0.003 [0.07]	0.274 [04.80]	0.003 [0.06]
μ^-	0.159 [03.06]	0.002 [0.05]	0.166 [02.90]	0.003 [0.05]
μ^+	0.185 [03.56]	0.002 [0.04]	0.184 [03.23]	0.003 [0.05]
π^-	0.003 [00.07]	0.000 [0.00]	0.004 [00.06]	0.000 [0.00]
π^+	0.004 [00.08]	0.000 [0.00]	0.005 [00.08]	0.000 [0.00]

variation in organ dose using a human anatomical phantom for Apollo 11 and Apollo 14 missions from trapped protons. Using a MC simulation procedure with simplified phantom model in X-ray radiation environment for medical purpose, Lewis et al. (1988) reported different absorption dose rates in different organs indicating a ratio more than factor of 2 between colon and stomach. In a recent study of organ dose estimation due to computed tomography, De Mattia et al. (2020) also reported substantial difference of radiation dose rates in different organs which also support our calculation. However, Reitz et al. (2012) reported more or less flat distribution of absorbed dose rate at different organs in human body at the radiation environment on moon with only high energy primary GCRs and using ICRP phantom model. We can speculate the differential organ doses due to radiation environment at the aviation altitude and organ material distribution in the phantoms (high density and relatively high Z bone material should play a role here). The direct verification of the obtained result is difficult due to lack of experimental knowledge and other calculations of dose rate for individual organs at this level. Some future development in this concern with computation or/and experiments can shed more light and verify the results obtained in the current calculation.

The sex-averaged absorbed (equivalent) dose rate on eye lens is calculated as 1.84 μGy/h (5.16 μSv/h). The equivalent dose limit of eye lens for occupational exposure and public exposure is 20 mSv and 15 mSv per year. So from this simulation, it can be seen that this limit can be exceeded for frequent fliers or aircrews which could increase the chance of eye cataracts. The absorbed dose rate and equivalent dose rate received by the prostate (uterus) of male (female) phantom is 1.25 (1.78) μGy/h and 1.82 (3.21) μSv/h. A recent study by Grajewski et al. (2015) suggests that the risk of miscarriage among the female flight attendant will increase for radiation dose of or more than 0.1 mGy in week 9–13 from conception. The estimated threshold dose for the gestational period can be found in Patel et al. (2007), which is quite high but can be reached during severe solar particle events, Terrestrial Gamma-ray Flash events (Dwyer et al., 2010) or frequent use of flights from high altitude or long haul polar routes. So,
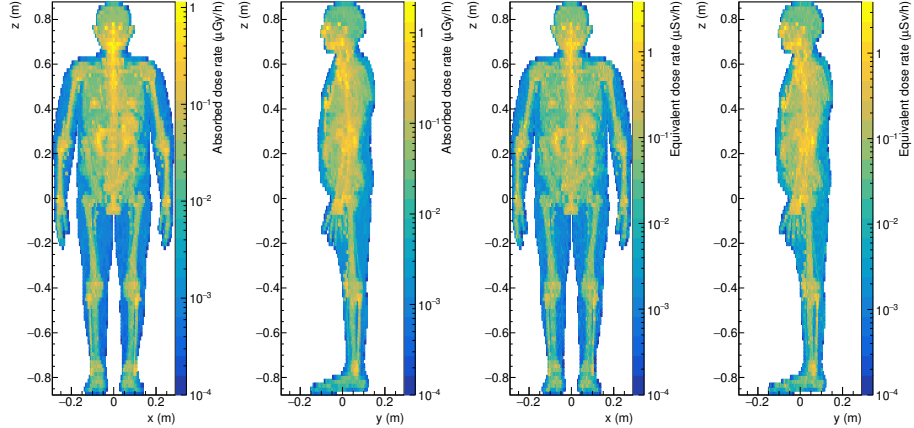
15

Figure 7: Spatial distribution (frontal view; side-wise view) of absorbed dose rate and equivalent dose rate in male phantom.

all frequently flying pregnant women or aircrews should take extra care of their fetus during their early gestation.

The incident energetic particles and radiation produce different sub-atomic secondary particles, as well as some radioactive nuclei, by interacting with the human body. These radioactive nuclei are mainly produced by spallation reaction of protons and activation by neutrons in our body (Brodzinski et al., 1969). The amount of radiation dose per hour imparted by these radionuclides is negligible, but can be accumulated to give substantial dose for extended exposure time or elevated radiation environment. Because of their radioactive nature, these cosmogenic radio-isotopes are particularly important, as they can be accumulated in some specific organs due to their physicochemical nature, where it could cumulatively give radiation dose depending upon their biological half-lives which may lead to stochastic detrimental effect like cancer. Despite of the harmful characteristics of the cosmogenic radionuclides, they could be used to accurately measure the radiation dose in the human body (Brodzinski et al., 1969). They have half-lives ranging from less than a second to years. Internal radioactivity is particularly dangerous than the external radiation as the de-
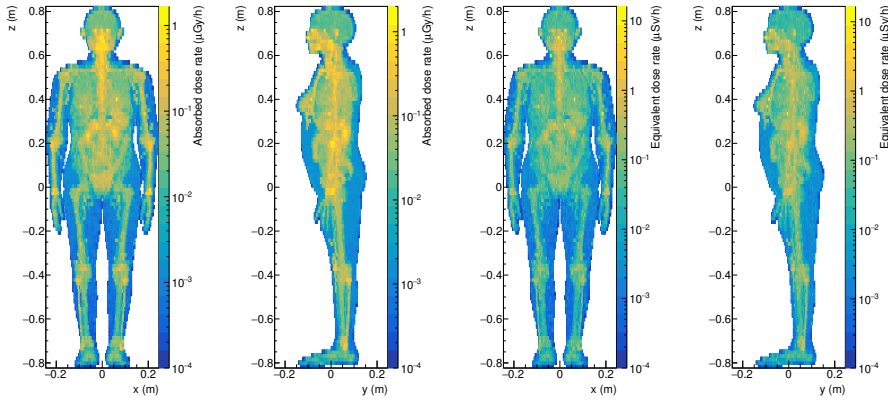
Figure 8: Spatial distribution (frontal view; side-wise view) of absorbed dose rate and equivalent dose rate in female phantom.
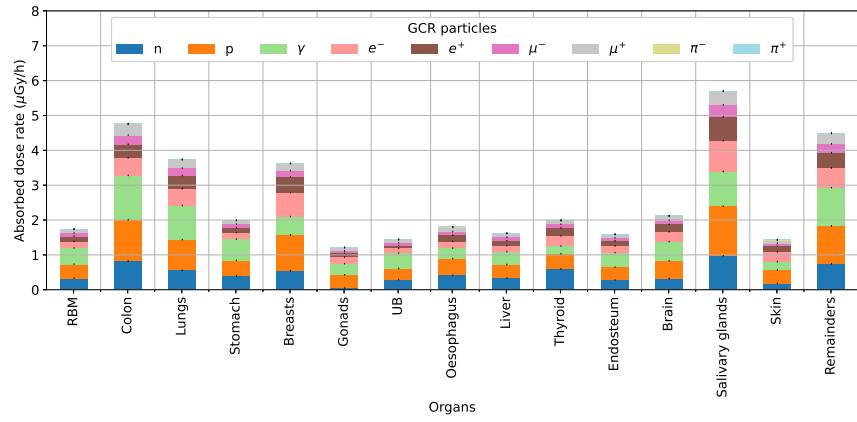

Figure 9: Absorbed dose rate for different incident particles in different organs of male phantom.
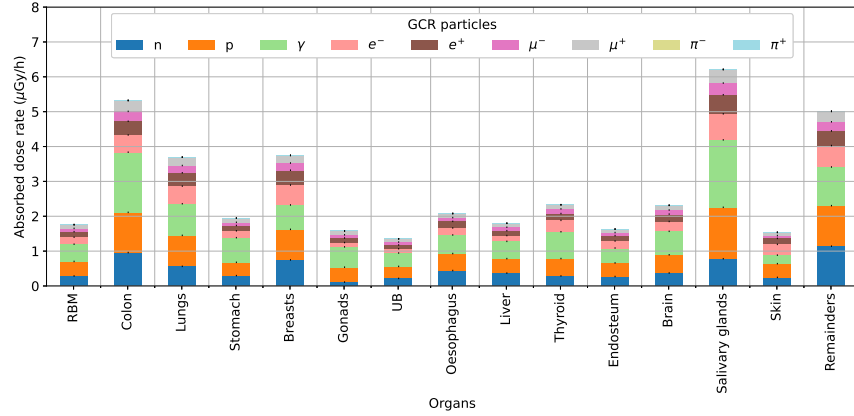
17

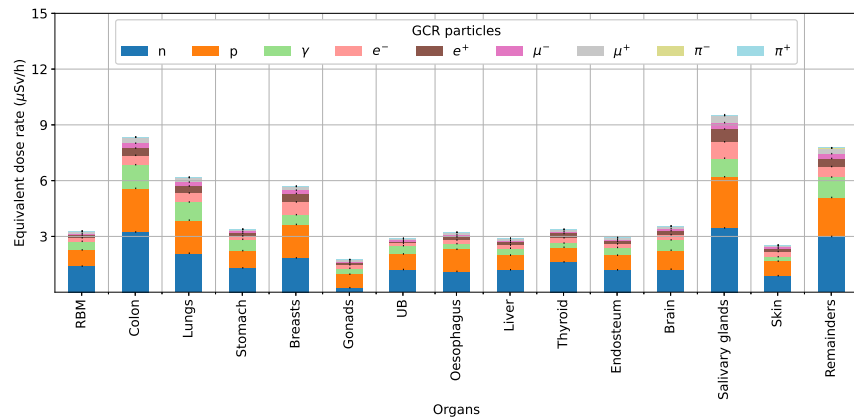Figure 10: Absorbed dose rate for different incident particles in different organs of female phantom.

Figure 11: Equivalent dose rate for different incident particles in different organs of male phantom.
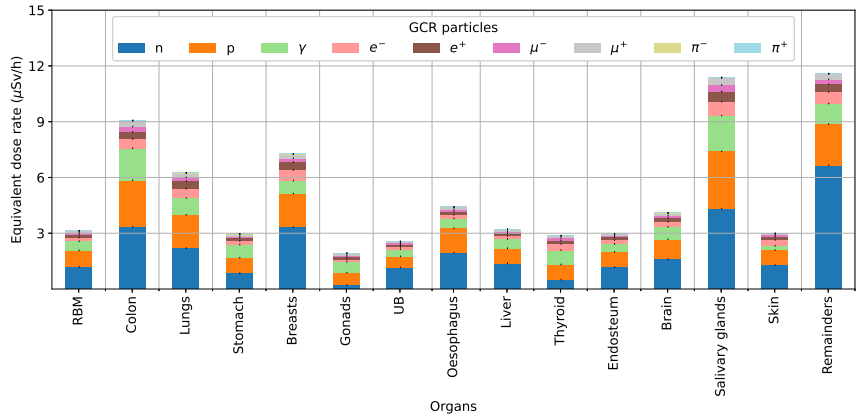
Figure 12: Equivalent dose rate for different incident particles in different organs of female phantom.

caying particles or radiations may kill nearby tissue, cells or damage the DNA structure. In the current simulation work we also have calculated the production of radioactive nuclei in human body due to high energy particles or radiation interactions. Most abundant nuclides among all the produced radionuclides in human body are listed in Table 2 along with their half-life, mode of production and abundance.

Based on this result, we tried to have a rough estimation of the maximum limit to the career exposure of the aircrews due to cosmogenic radionuclides listed in Table 2. For this purpose, we considered the decay of the induced radionuclides at their corresponding position of generation inside human body as obtained from the simulation and calculated the absorbed dose from different radionuclides. The total number of radionuclides accumulated in the body is calculated considering overall occupational exposure for 20 and 30 years with 1000 flight hours per year. The number of radionuclides that decay over the lifetime after the exposure (considering 50 years from the median age of occupational exposure suffered) to give the radiation dose, depending on the corresponding half lives of the radionuclides. This calculation yields the carrier exposure of about 6 mSv and 9 mSv considering 20 and 30 years of occupational exposures respec-

Table 2: Total production of cosmogenic radionuclides per hour inside phantoms from interaction of cosmic ray at aircraft altitude.

Radionuclide	Half-life	Mode of production*	Atoms/hour
^{14}C	5700 y	$^{14}N(n,p)^{14}C$	2.88×10^5
^{15}O	122.24 s	$^{16}O(n,2n)^{15}O$	1.24×10^5
^{36}Cl	3.01×10^5 y	$^{35}Cl(n,\gamma)^{36}Cl$	8.39×10^4
^{11}C	20.36 m	$^{12}C(n,2n)^{11}C$	6.59×10^4
^{7}Be	53.22 d	$^{12}C(n,2n+\alpha)^{7}Be$	3.20×10^4
^{40}K	1.24×10^9 y	$^{39}K(n,\gamma)^{40}K$	1.91×10^4
^{14}O	12.5 ms	$^{16}O(n,3n)^{14}O$	2.08×10^4
^{6}He	806.7 ms	$^{12}C(n,p+\alpha+d)^{6}He$	1.45×10^4
^{16}N	7.13 s	$^{16}O(n,p)^{16}N$	1.16×10^4
^{41}Ca	9.94×10^4 y	$^{40}Ca(n,\gamma)^{41}Ca$	1.25×10^4
^{10}Be	1.51×10^6 y	$^{12}C(n,2n+p)^{10}B$	1.27×10^4
^{12}B	20.20 ms	$^{16}O(n,p+\alpha)^{12}B$	6.75×10^3
^{13}N	9.96 m	$^{16}O(n,p+3n)^{13}N$	1.09×10^4
^{8}Li	839.9 ms	$^{12}C(n,p+\alpha)^{8}Li$	8.20×10^3
^{37}Ar	35.01 d	$^{40}Ca(n,\alpha)^{37}Ar$	6.97×10^3
^{12}N	11.0 ms	$^{16}O(n,p+4n)^{12}N$	5.75×10^3
^{32}P	14.26 d	$^{31}P(n,\gamma)^{32}P$	6.04×10^3
^{24}Na	14.99 h	$^{23}Na(n,\gamma)^{24}Na$	4.03×10^3

* Only major production processes

tively. However, it should be emphasized here that, this calculation is based on the physical half-lives of the radionuclides. But due to various reasons their biological half-lives would be different, which should be actually considered in the calculation. Again, the production rates of these radionuclides depends on the location (altitude/latitude) of exposure over the occupational career which also should be considered.

3.3. Radiation flux inside aircraft structure

The simulated flux of different secondary particles at three different positions inside the aircraft, along with the flux outside the aircraft structure (i.e., in the free atmosphere), for both downward and upward going particles can be seen from Fig. 13 and Fig. 14. Here, we discarded the downward going $\pi^{\pm}$ due to their negligible contribution to the total effective dose rate (see Table 1). The change (in %) of the integral flux (particles $m^{-2}sr^{-1}s^{-1}$) for different individual secondary particles (as well as for the total contribution) in both downward and upward directions at different positions inside the fuselage with respect to the corresponding flux outside the aircraft, is given in Table 3. The corresponding change (in μSv/h) in effective dose rate in human body is tabulated in Table 4. However, to calculate the effective dose rate at different positions inside the aircraft we considered the same fluence-to-dose-rate weighting factor obtained from the dose rate calculation in human phantom in the atmosphere as discussed in Sec. 3.2.

From these results, it is apparent that inside the aircraft fuselage the flux of downward going particles are increased in general (with exception for the muons). This may be attributed due to the secondary production by interaction of high energy particles with the aircraft materials have overwhelmed the absorption of the particles in the aircraft shell. On the other hand, a significant reduction of particle flux inside the fuselage for upward going particles is discernible from the results. Which is mainly due to the presence of the floor and central fuel tank. But, since downward particles contribute almost ∼96% to the total effective dose rate, while upward particles contribute only ∼4% (see

Table 3: Percentage changes of integral flux (Particles $m^{-2}sr^{-1}s^{-1}$) for total and individual different secondary GCR particles in front, middle and back section of the fuselage with respect to the free atmosphere.

Particles	Front (%)		Middle (%)		Back (%)	
	Down	Up	Down	Up	Down	Up
n	04.51	-11.53	13.74	-86.87	05.59	-10.70
p	00.28	-49.61	05.83	-88.52	03.10	-40.39
γ	04.14	-30.87	27.15	-88.20	04.59	-26.64
e^-	12.25	-78.56	16.91	-94.03	13.85	-70.34
e^+	16.37	-42.29	29.90	-67.18	18.06	-29.28
μ^-	-2.74	-15.86	01.77	-88.64	-1.20	-11.59
μ^+	-2.56	-17.36	01.02	-88.06	02.30	-11.02
Total	04.60	-29.58	24.76	-88.09	05.26	-25.62

Table 1), the reduction of upward particle flux could not effectively reduce the dose rate. In fact this calculation shows about 9.7% increase of total effective dose rate at the center of the fuselage compared to the free atmosphere, while effective dose rate due to neutrons increase by $\sim 6\%$. The neutron dose rate measurement inside RB57-F military aircraft shows about 10% increment in the radiation dose rate than outside the aircraft Singleterry Jr et al. (1999). In a previous calculation, Ferrari et al. (2005) reported qualitatively similar findings of slight increment (depending on the position along the fuselage) of radiation dose in side the aircraft due to downward radiation, while the contribution from the upward radiation decremented due to the presence of the fuel and cargo content. However, the dose rate inside the fuselage may also change due to absorption of radiation by the internal structures, seats, passengers and other high-Z materials, which can be studied by MC simulation with detailed geometrical structure of the aircraft from the manufacture and corresponding measurements on board the aircraft.

Figure 13: Particle flux for different downward going secondary GCR particles (proton, neutron, γ, e^-, e^+, μ^-, μ^+) at aviation altitude and in four different positions (outside:Atmosphere, front, middle and back side of the aircraft).
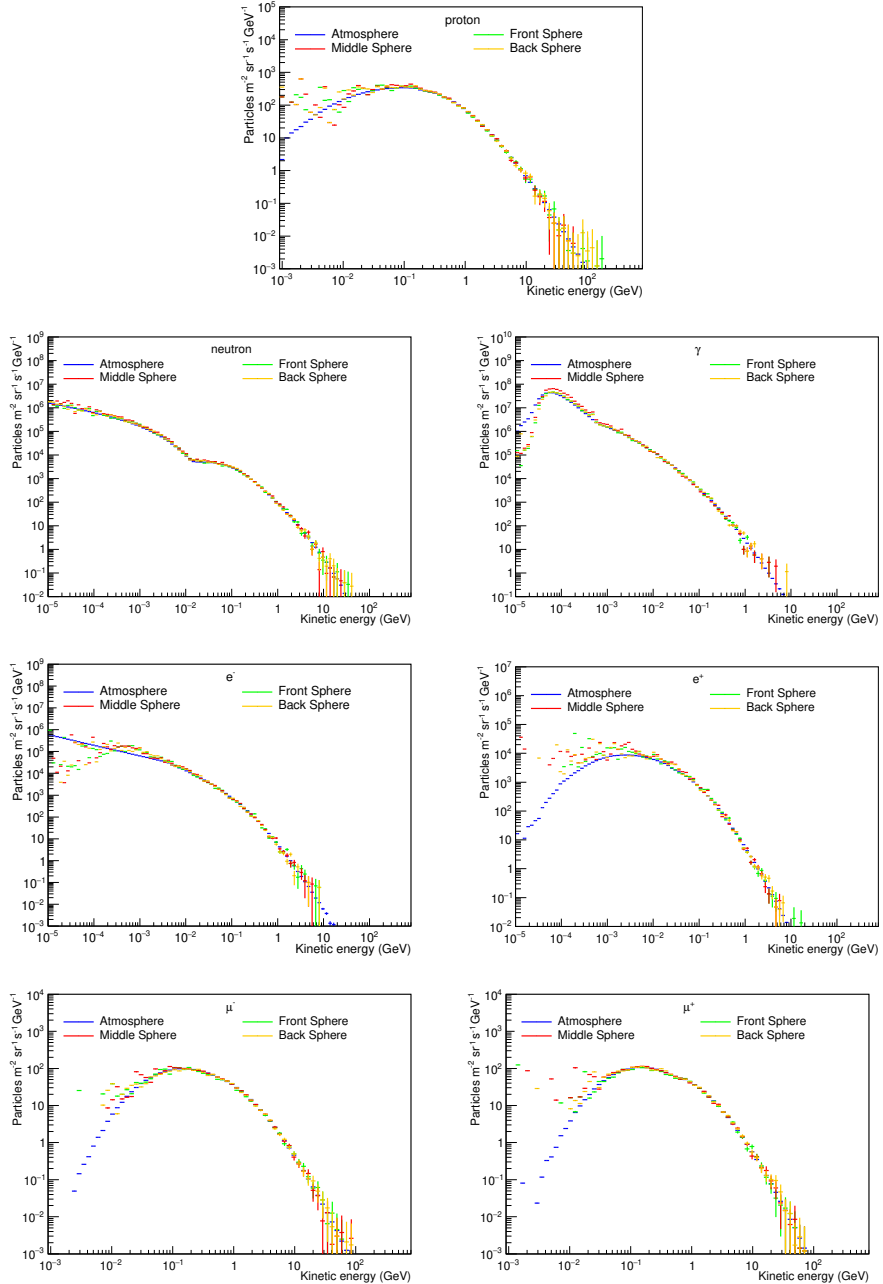
23

Figure 14: Particle flux for different upward going secondary GCR particles (proton, neutron, γ, e^-, e^+, μ^-, μ^+) at aviation altitude and in four different positions (outside:Atmosphere, front, middle and back side of the aircraft).
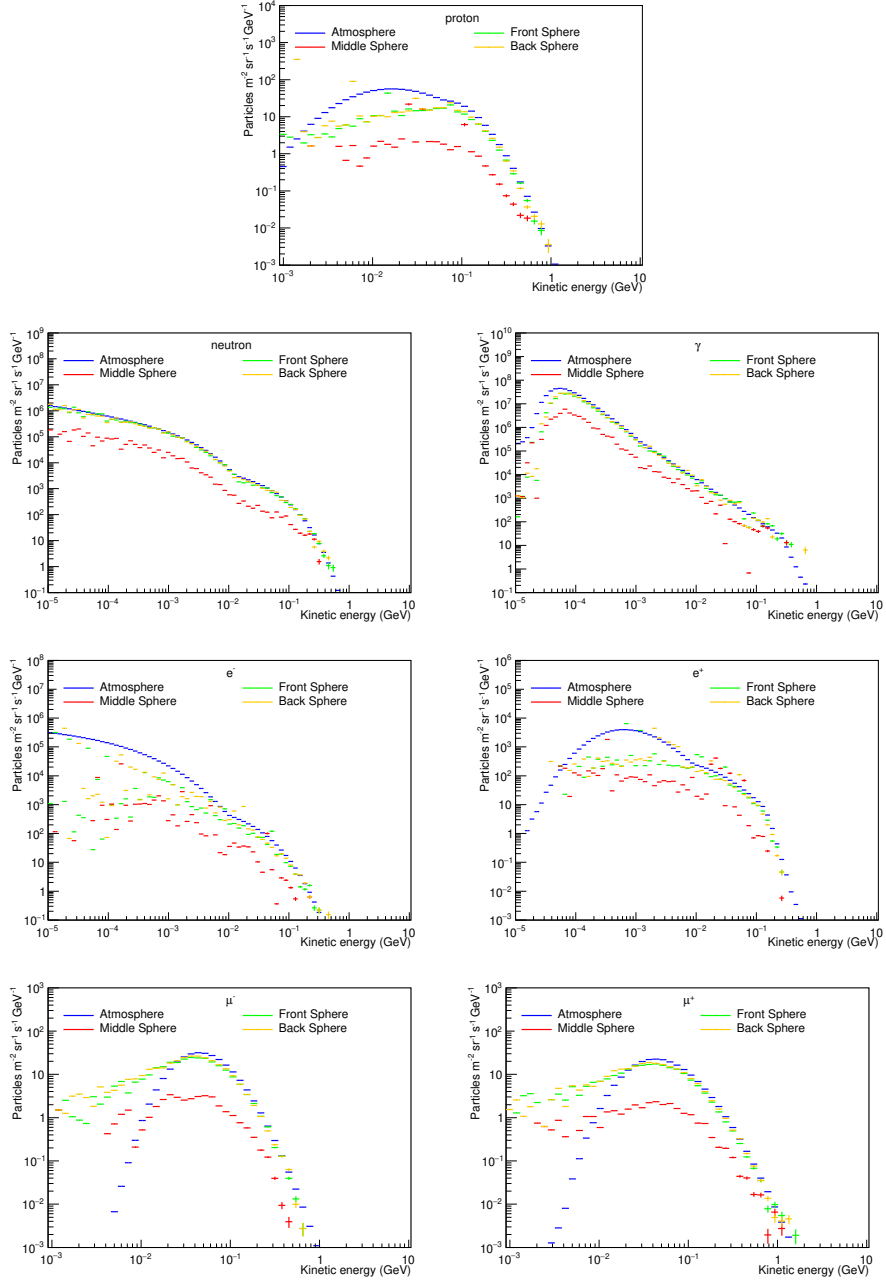
24

Table 4: Variation of effective dose rate for different downward and upward going secondary GCR particles inside the aircraft fuselage.

Particles	Front (μSv/h)		Middle (μSv/h)		Back (μSv/h)	
	Down	Up	Down	Up	Down	Up
n	0.0921	-0.0198	0.2808	-0.1493	0.1142	-0.0183
p	0.0040	-0.0042	0.0839	-0.0075	0.0446	-0.0034
γ	0.0313	-0.0075	0.2054	-0.0216	0.0347	-0.0065
e^-	0.0453	-0.0037	0.0626	-0.0045	0.0512	-0.0033
e^+	0.0454	-0.0015	0.0829	-0.0024	0.0501	-0.0010
μ^-	-0.0044	-0.0004	0.0028	-0.0027	-0.001	-0.0003
μ^+	-0.0047	-0.0004	0.0018	-0.0024	0.0042	-0.0003
Total	0.2091	-0.0379	0.7206	-0.1906	0.2973	-0.0334
	0.1712		0.5299		0.2638	

Table 5: Dose rate as calculated from this simulation and using the dose conversion coefficient from Pelliccioni (2000).

Particles	Effective dose rate ($\mu Sv/h$)	Effective dose rate* ($\mu Sv/h$)	Ambient dose equivalent* ($\mu Sv/h$)
n	2.2159	2.0371	2.2398
p	1.4486	2.1885	0.7790
γ	0.7812	0.4644	0.1895
e^-	0.3751	0.1924	0.1704
e^+	0.2811	0.1454	0.2507
μ^-	0.1660	0.0952	0.0935
μ^+	0.1880	0.1154	0.1108
π^-	0.0039	0.0023	0.0015
π^+	0.0048	0.0072	0.0054
Total	5.4651	5.2484	3.8408

* using fluence-to-dose conversion coefficients for isotropic irradiation

3.4. Comparison with previous dose calculations

This simulation yields that the total weighted sum of equivalent dose rate received by the female phantom is 5.72 μSv/h, whereas that by the male phantom is 5.20 μSv/h. So the sex-averaged effective dose rate is 5.46 μSv/h. The experimental or calculated dose rates received by the individual organs inside the human body (at aviation altitude), influenced by the aircraft structure at the geomagnetic latitude and altitude considered in this simulation are not available. So, we could not directly compare our simulated results for absorbed and equivalent dose rates on each organ of the male and female body. However, we bench-marked our simulation at different stages of the calculation.

In Sec. 3.1, we have already mentioned about the validation of the simulated proton flux at satellite altitude and atmospheric radiation flux at balloon altitude. We also compared the simulated neutron fluence rate at the aviation altitude with the experimental measurement reported by Goldhagen et al. (2002). Fig. 15 shows the neutron fluence rate per lethargy at 20 km altitude and in 1.0 - 1.1 rad geomagnetic latitude, as obtained in this simulation and compared to that measured by Goldhagen et al. (2002) in the same latitude and altitude region. Considering this neutron fluence and conversion coefficients from Pelliccioni (2000), we calculated the effective dose rate (ambient dose equivalent rate) as 7.60 (9.12) μSv/h which is within 10% deviation of the measured value.

The radiation dose in the human phantom depends on many factors like: material distribution considered in the phantom, incident radiation spectra, energy range of the radiation, angular distribution of the incident flux etc. For example, Sato et al. (2009) showed the effect of using different source geometries on radiation dose. Here, in this work, instead of using fluence to dose conversion coefficients, using micro-dosimetric technique we explicitly calculated the energy depositions in different organs for a wide range of radiation types and energy considering different angular distributions for downward and upward radiations. However, to compare our simulated dose rate, we also calculated the effective dose rate using the common conversion coefficients for isotropic irradiation from Pelliccioni (2000) and the values for different radiation types are tabulated in
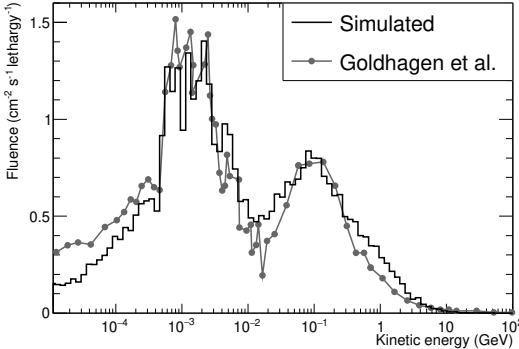
26

Figure 15: Neutron fluence rate at 20 km altitude and in 1.0 - 1.1 rad geomagnetic latitude obtained in this simulation (black) and that measured by Goldhagen et al. (2002) (gray).

Table 5. The comparison shows that the total effective dose rate are within the acceptable uncertainty range, although some deviations in the effective dose rate for different particles are noticeable due to above mentioned factors.

Since, effective dose and equivalent dose are not measurable quantities, so ambient dose equivalent ($H^*(10)$) used instead for measurements. In Table 5 we also presented the $H^*(10)$ values for different particles calculated using corresponding conversion coefficients. The apparent underestimation of total ambient dose equivalent rate compared to the total effective dose rate can be understandable from the measurement of dose depth distribution aboard a series of flights from Cologne (GER) to Washington, DC (USA) using a quasi tissue-equivalent phantom sphere by Vana et al. (2003). This measurement shows that the maximum dose equivalent appears in a depth of 50 to 60 mm rather than 10 mm, implying that $H^*(10)$ underestimates the actual whole-body radiation exposure. Similarly, Petoussi-Henss et al. (2010); Veinot & Hertel (2011) showed that above few MeV, $H^*(10)$ can not provide a conservative estimate of the protection quantities. In fact, whether $H^*(10)$ saturates with energy, effective dose increases. Ferrari & Pelliccioni (1998) also conclude that the only up to a limited energy range $H^*(10)$ gives a conservative estimate of effective dose and for high energy neutrons. For the validation of this simulation here we

27

also compere the calculated ambient dose equivalent rate (3.84 $\mu Sv/h$) in the simulated region ($\theta_M = 45°$–$50°$, Altitude $= 10$ km, $\phi = 524$ MV) with the other reported values of ambient dose equivalent rate in Ploc et al. (2013); Lindborg et al. (2004b); Bottollier-Depois et al. (2012); Lindborg et al. (2004a) which is determined by in-flight measurements through several radiation monitors and in different altitude, latitude as well as solar condition. We simply interpolate the reported values for the comparison, which shows that our simulated dose rate is well within the acceptable limit of 30% uncertainty.

4. Conclusions

The gender specific radiation dose on the human body and its internal organs are calculated in this work through MC simulation, using most updated models describing the atmosphere and magnetosphere, CR flux, human phantoms and organ specific weighting factors. The calculation shows that, among all the incident primary particles, most of the radiation effective dose received by the human body is due to the neutrons, at the location of aviation altitude considered in this simulation. By interacting with the human phantoms secondary CRs also produce different cosmogenic radioactive nuclides with half lives ranging from less than a second to years. These radionuclides may give negligible contributions to the total effective dose received per hour during the flight, but can gradually increase with increasing altitude, latitude and exposure time and most importantly can have significant cumulative effect over the human lifespan. The calculation also reveals that the dose received by the human phantoms at flight altitude are mostly due to downward directed particles with a small contribution by the upward particles. Comparison of the calculated effective dose rate in this work with that calculated by various other computer codes and measurement as reported in Ploc et al. (2013); Lindborg et al. (2004b); Bottollier-Depois et al. (2012); Lindborg et al. (2004a) shows an agreement well within the acceptable error limit. Study of the shielding effect of the aircraft structure on the radiation dose is very important in aviation safety as this helps

us to better predict radiation dose for radiological protection. By considering a detailed aircraft structure Battistoni et al. (2005) showed that, inside the aircraft, decrease of ambient dose equivalent is more significant than the decrease of effective dose compared to free atmosphere. Based on this they conclude that effective dose at the free atmosphere can be used for individuals risk assessment. On the other hand great care should be taken to consider the shielding effect on the ambient dose equivalent when compared the calculated value with the measurement. Here, in this simulation, the consideration of the simplified aircraft model structure with only the outer shell, gives apparently odd result that the effective radiation dose is increased inside the aircraft. But this is understandable from the fact that the high-energy particle fluxes are converted to relatively low-energy particles by the shell material which subsequently contribute to the received dose by the human body more efficiently. However, this calculation can be improved by considering the the actual particle flux distribution produced inside the aircraft to calculate the energy depositions in the phantoms, rather than using the fluence-to-dose-rate weighting coefficients obtained from the calculation at the atmosphere outside the aircraft. Moreover, the calculation of radiation dose in human body inside the aircraft can further be improved by considering more realistic internal structure of the aircraft and passenger distribution, which is of course practically very challenging to implement in this kind of simulation.

5. Acknowledgment

References

Adriani, O., Barbarino, G., Bazilevskaya, G., Bellotti, R., Boezio, M., Bogomolov, E., Bongi, M., Bonvicini, V., Borisov, S., Bottai, S. et al. (2013).

Time dependence of the proton flux measured by PAMELA during the 2006 July-2009 December solar minimum. *The Astrophysical Journal*, *765*(2), 91.

Agostinelli, S., Allison, J., Amako, K. a., Apostolakis, J., Araujo, H., Arce, P., Asai, M., Axen, D., Banerjee, S., Barrand, G. . et al. (2003). GEANT4—a simulation toolkit. *Nuclear instruments and methods in physics research section A: Accelerators, Spectrometers, Detectors and Associated Equipment*, *506*(3), 250–303.

Aguilar, M., Aisa, D., Alpat, B., Alvino, A., Ambrosi, G., Andeen, K., Arruda, L., Attig, N., Azzarello, P., Bachlechner, A. et al. (2015). Precision measurement of the proton flux in primary cosmic rays from rigidity 1 GV to 1.8 TV with the Alpha Magnetic Spectrometer on the International Space Station. *Physical Review Letters*, *114*(17), 171103.

Alves, M. C., Galeano, D. C., Santos, W. S., Lee, C., Bolch, W. E., Hunt, J. G., da Silva, A. X., & Carvalho, A. B. (2016). Comparison of the effective dose rate to aircrew members using hybrid computational phantoms in standing and sitting postures. *Journal of Radiological Protection*, *36*(4), 885–901.

Aspholm, R., Lindbohm, M.-L., Paakkulainen, H., Taskinen, H., Nurminen, T., & Tiitinen, A. (1999). Spontaneous abortions among Finnish flight attendants. *Journal of occupational and environmental medicine*, *41*(6), 486–491.

Banjac, S., Heber, B., Herbst, K., Berger, L., & Burmeister, S. (2019). On-the-Fly Calculation of Absorbed and Equivalent Atmospheric Radiation Dose in A Water Phantom with the Atmospheric Radiation Interaction Simulator (AtRIS). *Journal of Geophysical Research: Space Physics*, *124*(12), 9774–9790.

Battistoni, G., Ferrari, A., Pelliccioni, M., & Villari, R. (2005). Evaluation of the doses to aircrew members taking into consideration the aircraft structures. *Advances in Space Research*, *36*(9), 1645–1652.

Bazilevskaya, G., & Svirzhevskaya, A. (1998). On the stratospheric measurements of cosmic rays. *Space Science Reviews*, *85*(3-4), 431–521.

Bennett, L., Lewis, B., Bennett, B., McCall, M., Bean, M., Doré, L., & Getley, I. (2013). A survey of the cosmic radiation exposure of Air Canada pilots during maximum galactic radiation conditions in 2009. *Radiation measurements*, *49*, 103–108.

Boeing Co. (2020). Boeing 777-200LR / -300ER / -FreighterAirplane Characteristics for Airport Planning. `http://www.boeing.com/assets/pdf/commercial/airports/acaps/777_2lr3er.pdf`. [Online; accessed 02–April–2020].

Bottollier-Depois, J.-F., Beck, P., Latocha, M., Mares, V., Matthiä, D., Rühm, W., & Wissmann, F. (2012). Comparison of codes assessing radiation exposure of aircraft crew due to galactic cosmic radiation. *EURADOS report 2012-03*, (pp. 1–55). ISBN 978-3-943701-02-9.

Brodzinski, R., Wogman, N., & Perkins, R. (1969). Cosmic-ray induced radioactivity in astronauts as a measure of radiation dose. *Space life sciences*, *1*(4), 545–553.

Caballero-Lopez, R., & Moraal, H. (2004). Limitations of the force field equation to describe cosmic ray modulation. *Journal of Geophysical Research: Space Physics*, *109*(A1).

De Mattia, C., Campanaro, F., Rottoli, F., Colombo, P. E., Pola, A., Vanzulli, A., & Torresin, A. (2020). Patient organ and effective dose estimation in ct: comparison of four software applications. *European radiology experimental*, *4*(1), 1–16.

Dwyer, J., Smith, D., Uman, M., Saleh, Z., Grefenstette, B., Hazelton, B., & Rassoul, H. (2010). Estimation of the fluence of high-energy electron bursts produced by thunderclouds and the resulting radiation doses received in aircraft. *Journal of Geophysical Research: Atmospheres*, *115*(D9).

Dyer, C., & Lei, F. (2001). Monte Carlo calculations of the influence on air-craft radiation environments of structures and solar particle events. *IEEE Transactions on Nuclear Science*, *48*(6), 1987–1995.

Dyer, C., Lei, F., Clucas, S., Smart, D., & Shea, M. (2003). Calculations and observations of solar particle enhancements to the radiation environment at aircraft altitudes. *Advances in Space Research*, *32*(1), 81–93.

Ferrari, A., & Pelliccioni, M. (1998). Fluence to dose equivalent conversion data and effective quality factors for high energy neutrons. *Radiation Protection Dosimetry*, *76*(4), 215–224.

Ferrari, A., Pelliccioni, M., & Pillon, M. (1997). Fluence to effective dose conversion coefficients for neutrons up to 10 TeV. *Radiation Protection Dosimetry*, *71*(3), 165–173.

Ferrari, A., Pelliccioni, M., & Villari, R. (2004). Evaluation of the influence of aircraft shielding on the aircrew exposure through an aircraft mathematical model. *Radiation protection dosimetry*, *108*(2), 91–105.

Ferrari, A., Pelliccioni, M., & Villari, R. (2005). A mathematical model of aircraft for evaluating the effects of shielding structure on aircrew exposure. *Radiation protection dosimetry*, *116*(1-4), 331–335.

Gaisser, T. K. (1990). *Cosmic rays and particle physics.*. Cambridge University Press.

Geant4 (2020). Physics list guide. `http://geant4-userdoc.web.cern.ch/geant4-userdoc/UsersGuides/PhysicsListGuide/html/reference_PL/QGSP_BIC.html`. [Online; accessed 02–April–2020].

Goldhagen, P., Reginatto, M., Kniss, T., Wilson, J., Singleterry, R., Jones, I., & Van Steveninck, W. (2002). Measurement of the energy spectrum of cosmic-ray induced neutrons aboard an ER-2 high-altitude airplane. *Nuclear Instruments and Methods in Physics Research Section A: Accelerators, Spectrometers, Detectors and Associated Equipment*, *476*(1-2), 42–51.

Gopalswamy, N., Mewaldt, R., & Torsti, J. (2006). Solar eruptions and energetic particles: An introduction. *Solar Eruptions and Energetic Particles*, (165), 1–5.

Grajewski, B., Whelan, E. A., Lawson, C. C., Hein, M. J., Waters, M. A., Anderson, J. L., MacDonald, L. A., Mertens, C. J., Tseng, C.-Y., Cassinelli, R. T. et al. (2015). Miscarriage among flight attendants. *Epidemiology (Cambridge, Mass.)*, *26*(2), 192.

Griffin, K. T., Mille, M. M., Pelletier, C., Gopalakrishnan, M., Jung, J. W., Lee, C., Kalapurakal, J., Pyakuryal, A., & Lee, C. (2019). Conversion of computational human phantoms into DICOM-RT for normal tissue dose assessment in radiotherapy patients. *Physics in Medicine & Biology*, *64*(13), 13NT02.

Herbst, K., Muscheler, R., & Heber, B. (2017). The new local interstellar spectra and their influence on the production rates of the cosmogenic radionuclides 10Be and 14C. *Journal of Geophysical Research: Space Physics*, *122*(1), 23–34.

ICAO (2016). Global air navigation plan 2016–2030. `https://www.icao.int/airnavigation/documents/ganp-2016-interactive.pdf`. [Online; accessed 02–April–2020].

ICRP (1991). 1990 recommendations of the International Commission on Radiological Protection. ICRP publication 60. *Annals of the ICRP*, *21*, 1–3.

ICRP (2007). The Recommendations of the International Commission on Radiological Protection. ICRP Publication 103. *Annals of the ICRP*, *37*, 2–4.

ICRU (2010). Reference Data for the Validation of Doses from Cosmic-radiation Exposure of Aircraft Crew. ICRU Report 84 (prepared jointly with ICRP). *Journal of the ICRU*, *10*(2).

Lauria, L., Ballard, T. J., Caldora, M., Mazzanti, C., & Verdecchia, A. (2006). Reproductive disorders and pregnancy outcomes among female flight attendants. *Aviation, space, and environmental medicine*, *77*(5), 533–539.

Lee, C., Lodwick, D., Hurtado, J., Pafundi, D., Williams, J. L., & Bolch, W. E. (2009). The UF family of reference hybrid phantoms for computational radiation dosimetry. *Physics in Medicine & Biology*, *55*(2), 339.

Lewis, C., Smith, P., Stratton, I., Darby, S., & Doll, R. (1988). Estimated radiation doses to different organs among patients treated for ankylosing spondylitis with a single course of x rays. *The British journal of radiology*, *61*(723), 212–220.

Lindborg, L., Bartlett, D., Beck, P., McAulay, I., Schnuer, K., Schraube, H., & Spurny, F. (2004a). *Cosmic radiation exposure of aircraft crew: compilation of measured and calculated data*. EC Report Radiation Protection 140. Final Report of EURADOS WG 5, Luxembourg, pp. 1–271 (ISBN 92-894-8448-9).

Lindborg, L., Bartlett, D., Beck, P., McAulay, I., Schnuer, K., Schraube, H., & Spurny, F. (2004b). Cosmic radiation exposure of aircraft crew: compilation of measured and calculated data. *Radiation protection dosimetry*, *110*(1-4), 417–422.

Lund, M., & Jevremovic, T. (2019). Enhanced GEANT4 Monte Carlo simulations of the space radiation effects on the International Space Station and Apollo missions using high-performance computing environment. *Acta Astronautica*, *165*, 219–228.

Moraal, H. (2013). Cosmic-ray modulation equations. *Space Science Reviews*, *176*(1-4), 299–319.

Patel, S. J., Reede, D. L., Katz, D. S., Subramaniam, R., & Amorosa, J. K. (2007). Imaging the pregnant patient for nonobstetric conditions: algorithms and radiation dose considerations. *Radiographics*, *27*(6), 1705–1722.

Pelliccioni, M. (2000). Overview of fluence-to-effective dose and fluence-to-ambient dose equivalent conversion coefficients for high energy radiation calculated using the fluka code. *Radiation Protection Dosimetry*, *88*(4), 279–297.

Petoussi-Henss, N., Bolch, W., Eckerman, K., Endo, A., Hertel, N., Hunt, J., Pelliccioni, M., Schlattl, H., & Zankl, M. (2010). ICRP Publication 116. Conversion coefficients for radiological protection quantities for external radiation exposures. *Annals of the ICRP*, *40*(2-5), 1–257.

Picone, J., Hedin, A., Drob, D. P., & Aikin, A. (2002). NRLMSISE-00 empirical model of the atmosphere: Statistical comparisons and scientific issues. *Journal of Geophysical Research: Space Physics*, *107*(A12), SIA–15.

Ploc, O., Ambrozova, I., Kubancak, J., Kovar, I., & Dachev, T. P. (2013). Publicly available database of measurements with the silicon spectrometer liulin onboard aircraft. *Radiation measurements*, *58*, 107–112.

Reames, D. V. (1999). Particle acceleration at the Sun and in the heliosphere. *Space Science Reviews*, *90*(3-4), 413–491.

Regener, E., & Pfotzer, G. (1934). Intensity of the cosmic ultra-radiation in the stratosphere with the tube-counter. *Nature*, *134*(3383), 325–325.

Reitz, G., Berger, T., & Matthiae, D. (2012). Radiation exposure in the moon environment. *Planetary and Space Science*, *74*(1), 78–83.

Sarkar, R., Chakrabarti, S. K., Pal, P. S., Bhowmick, D., & Bhattacharya, A. (2017). Measurement of secondary cosmic ray intensity at Regener-Pfotzer height using low-cost weather balloons and its correlation with solar activity. *Advances in Space Research*, *60*(5), 991–998.

Sarkar, R., Roy, A., & Chakrabarti, S. K. (2020). Simulation of cosmic rays in the Earth's atmosphere and interpretation of observed counts in an X-ray detector at balloon altitude near tropical region. *Advances in Space Research*, *65*(1), 189–197.

Sato, O., Yoshizawa, N., Takagi, S., Iwai, S., Uehara, T., Sakamoto, Y., Yamaguchi, Y., & Tanaka, S.-i. (1999). Calculations of effective dose and ambient dose equivalent conversion coefficients for high energy photons. *Journal of nuclear science and technology*, *36*(11), 977–987.

Sato, T., Endo, A., Zankl, M., Petoussi-Henss, N., & Niita, K. (2009). Fluence-to-dose conversion coefficients for neutrons and protons calculated using the phits code and icrp/icru adult reference computational phantoms. *Physics in Medicine & Biology*, *54*(7), 1997.

Singleterry Jr, R. C., Shinn, J. L., Wilson, J. W., Maiden, D. L., Thibeault, S. A., Badavi, F. F., Conroy, T., & Braby, L. (1999). Aircraft Radiation Shield Experiments—Preflight Laboratory Testing. NASA STI/Recon Technical Report N. `https://citeseerx.ist.psu.edu/viewdoc/download?doi=10.1.1.39.4978&rep=rep1&type=pdf`.

Stone, E., Cummings, A., McDonald, F., Heikkila, B., Lal, N., & Webber, W. (2013). Voyager 1 observes low-energy galactic cosmic rays in a region depleted of heliospheric ions. *Science*, *341*(6142), 150–153.

Störmer, C. (1955). *The polar aurora*. Clarendon Press.

Thébault, E., Finlay, C. C., Beggan, C. D., Alken, P., Aubert, J., Barrois, O., Bertrand, F., Bondar, T., Boness, A., Brocco, L. et al. (2015). International geomagnetic reference field: the 12th generation. *Earth, Planets and Space*, *67*(1), 79.

Tsyganenko, N., & Andreeva, V. (2016). An empirical RBF model of the magnetosphere parameterized by interplanetary and ground-based drivers. *Journal of Geophysical Research: Space Physics*, *121*(11), 10–786.

Vana, N., Hajek, M., & Berger, T. (2003). Ambient dose equivalent H*(d)-an appropriate philosophy for radiation monitoring onboard aircraft and in space?. IRPA Regional Congress on Radiation Protection in Central Europe, (p. 573). Slovakia: Nuclear Regulatory Authority of the Slovak Republic. `https://inis.iaea.org/collection/NCLCollectionStore/_Public/36/097/36097704.pdf`.

Veinot, K., & Hertel, N. (2011). Personal dose equivalent conversion coefficients for photons to 1 gev. *Radiation protection dosimetry*, *145*(1), 28–35.

Vos, E. E., & Potgieter, M. S. (2015). New modeling of galactic proton modulation during the minimum of solar cycle 23/24. *The Astrophysical Journal*, *815*(2), 119.